Dynamical imprints on precipitation cluster statistics across a hierarchy of high-resolution simulations

Claudia Christine Stephan[1] and Bjorn Stevens[2]

[1]Leibniz Institute of Atmospheric Physics at the University of Rostock, Kühlungsborn, Germany
[2]Max Planck Institute for Meteorology, Hamburg, Germany

Correspondence: Claudia Christine Stephan (ccstephan@iap-kborn.de)

Abstract. Tropical precipitation cluster area and intensity distributions follow power laws, but the physical processes responsible for this macroscopic behavior remain unknown. We analyze global simulations at ten-kilometer horizontal resolution that are configured to have drastically varying degrees of realism, ranging from global radiative-convective equilibrium to fully realistic atmospheric simulations, to investigate how dynamics influence precipitation statistics. We find the presence of stirring and large-scale vertical overturning, as associated with substantial planetary and synoptic-scale variability, to be key for having cluster statistics approach power laws. The presence of such large-scale dynamics is reflected in steep vertical velocity spectra. Large-scale rising and sinking modulate the column water vapor and temperature field, leading to a heterogeneous distribution of moist and dry patches and regions of strong mass flux, in which large precipitation clusters form. Our findings suggest that power laws in Earth's precipitation cluster statistics stem from the robust power laws of atmospheric motions.

1 Introduction

The majority of tropical precipitation clusters follow scale-free frequency distributions for integrated rain rates (Peters et al., 2010; Quinn and Neelin, 2017a) and cluster sizes (Teo et al., 2017). High-resolution simulations (Quinn and Neelin, 2017a) and Coupled Model Intercomparison Project Phase 5 models (Quinn and Neelin, 2017b) also produce scale free distributions across a wide range of scales. The spectral range over which scale free behavior (or power-law scaling) applies tends to increase with warming. However, the physical origin of the cluster scaling laws remains elusive and motivates our study.

Mathematically, the cluster scaling laws have been described from the perspective of self-organizing criticality (Teo et al., 2017) and percolation theory (Peters and Neelin, 2006; Peters et al., 2009). While these concepts rest on sound mathematical foundations, they do not provide insights on underlying physical mechanisms. Previous studies tried to elucidate the physical processes that matter for the cluster scalings. For instance, Ahmed and Neelin (2019) developed a spatially two-dimensional model (horizontal plane) that represented a number of processes, from the effects of large scale circulation to internal dynamics associated with storm systems. This model combined the weak temperature gradient energy equations with an empirically motivated precipitation parameterization and thus allowed a large variety of sensitivity test. The model reproduced power-law scaling for realistic model parameter ranges. In our study we use a model that does not rely on empirical representations of the crucial process of moist convection. We focus on exploring the emergence of scaling laws across different planetary configu-

25 rations. We perform thirteen one-year long global simulations with the Icosahedral Nonhydrostatic model ICON (Hohenegger et al., 2023). The configurations we investigate range from global radiative-convective equilibrium (RCE) simulations to more complex simulations with prescribed sea surface temperatures (SSTs) and land. A relatively coarse horizontal resolution of 10 km allows for long integrations, a requirement for sampling the tails in the distributions. We turn convective parameterizations off to explicitly model the main processes responsible for the evolution of the column water vapor (CWV) field.

30 Focusing on the CWV field is inspired by the study of Li et al. (2022). They performed an aquaplanet simulation and obtained so-called "CWV islands" by cutting the CWV field at the critical moisture value that triggers precipitation. The "island area" is the number of connected pixels exceeding the threshold. The "island volume" is the total CWV above this threshold. They demonstrated that the areas of these islands agree well with the areas of precipitation clusters, which is of course expected. The same holds for the island volume and area-integrated precipitation, as is also expected. Unexpected was that CWV islands

35 followed scaling laws for a wide range of moisture thresholds: Even when cut at rather dry thresholds where there is no precipitation, the island volumes and areas followed similar scaling laws as if cut at wet thresholds. From a mathematical point of view, this implies that the CWV field must be approximately "self-affine", i.e. upon zooming in or out, it looks the same after re-scaling the overall amplitude. The height of a self-affine surface is described by $z(\boldsymbol{x}) \sim b^{-h}z(b\boldsymbol{x})$, where $\boldsymbol{x}$ is a location in space, b is a rescaling factor, h is the "roughness exponent" and '$\sim$' denotes statistical equivalence. The roughness exponent

40 h sets the slope of the scaling laws. In other words, it determines how many big clusters should exist for a given number of small clusters or vice versa. Previous work also demonstrated scale free behavior in water vapor variability (Schemann et al., 2013).

As mentioned in the study of Li et al. (2022), the observed h for precipitation clusters is close to the universal prediction of the Kardar-Parisi-Zhang (KPZ) equation. Pelletier (1997) noticed this for statistics of cumulus clouds and both studies

45 suggested that KPZ dynamics could be of relevance. The KPZ equation describes the positive growth of a surface $z(\boldsymbol{x},t)$ in the presence of Gaussian white noise $\eta(\boldsymbol{x},t)$ with a positive mean value. In a frame moving with the surface, the equation reads

$$\frac{\partial z}{\partial t} = \nu\nabla^2 z + \frac{\lambda}{2}(\nabla z)^2 + \eta, \tag{1}$$

where ν and λ are constants. In two spatial dimensions plus time, the solution to the KPZ equation is a surface with $h \approx 0.3867$ (Kardar et al., 1986; Pagnani and Parisi, 2015). Even though the modeling study of Ahmed and Neelin (2019), discussed above,

50 could not isolate a clear physical mechanism to explain the cluster scaling laws, it demonstrated that the observed scalings can be obtained in a spatially two-dimensional model, i.e. without explicitly considering the vertical dimension. If the KPZ equation is applicable to Earth's atmosphere, then this implies that Earth's atmospheric perturbations must match the required structure of the noise term η. In this study we consider atmospheres that differ substantially in their dynamic characteristics. The planetary configuration determines the scaling behavior of the atmospheric motion field. Our main result is that self affinity

55 in the CWV field and scaling laws in precipitation clusters only emerge in atmospheres with large-scale mixing.

Section 2 describes our data and methods, Section 3 presents the results, and Section 4 contains a brief conclusion.

2 Data and methods

2.1 Numerical simulations

All simulations have a 10 km horizontal grid spacing and 75 terrain-following height levels with a model top at 48 km. A
60 Rayleigh damping layer starts at 19 km. Microphysics, radiation and turbulence use the default Sapphire physics schemes
(Hohenegger et al., 2023). Although a horizontal resolution of 10 km may be generally thought to be too coarse to explicitly
represent convection, a number of studies show that it better and more physically represents convective processes than existing
parameterizations (Holloway et al., 2012; Vergara-Temprado et al., 2020; Takasuka et al., 2024).

CTL is the control simulation, which is initialized on January 1, 1979 from IFS operational analysis and has daily varying
65   prescribed SSTs interpolated from the monthly SST and sea ice concentration boundary conditions for AMIP II simu-
      lations (Taylor et al., 2000). Globally and annually averaged concentrations of greenhouse gases (Meinshausen et al.,
      2016) are prescribed from values taken from the respective year. Ozone is included with year 2014 values and varies
      spatially on a grid with $2.5°$ resolution in longitude and $1.675°$ resolution in latitude and on a monthly timescale, based
      on input4MIPS data. Aerosols are specified from a climatological data set (Kinne, 2019), which provides monthly data
70   on a $1°$ grid. External physical parameters for the land surface are based on Hagemann and Stacke (2015). The CTL
      simulation is a member of one of three classes of simulations. The remaining twelve simulations differ as follows.

CTL$_{\mathrm{zm}}$ is like CTL except that it uses constant and zonally averaged SSTs, which correspond to the time-averaged zonal-mean
      SSTs of CTL. Land is like in CTL. CTL and CTL$_{\mathrm{zm}}$ are the only simulations with a diurnal and annual cycle.

RCE is a radiative-convective equilibrium (RCE) simulation, i.e. non-rotating with constant insolation. It follows the 300 K
75   RCEMIP protocol (Wing et al., 2018).

RCE$_{\mathrm{s}}$ is like RCE but has the meridionally varying 'Qobs' SST profile (Neale and Hoskins, 2000) with a maximum SST of
      $27°C$ at the equator that decreases to a minimum SST of $0°C$ which is held fixed poleward of $60°$ in each hemisphere.

RCE$_{\mathrm{f}}$ is like RCE but rotates at the angular velocity of Earth.

RCE$_{\mathrm{r}}$ is like RCE but rotating with the Coriolis parameter set globally to its value at $45°$N.

80 **AP** is an aquaplanet (AP) simulation that combines RCE$_{\mathrm{f}}$ and RCE$_{\mathrm{s}}$, i.e. it rotates like Earth and the SST is prescribed
      following RCE$_{\mathrm{s}}$. Six additional AP simulations are performed:

AP$_{\mathrm{t+}}$ and AP$_{\mathrm{t-}}$ are like AP but with +5 or -5 K added to the SST everywhere including the poles.

AP$_{\mathrm{g+}}$ and AP$_{\mathrm{g-}}$ have gravity increased or decreased, respectively, by 20% relative to 9.81 m s^{-2}. This changes the dry
      adiabatic lapse rate $\mathrm{d}T/\mathrm{d}z = -g/c_p$, with T temperature, z height and c_p the isobaric specific heat capacity.

85 **AP$_{\mathrm{fg+}}$ and AP$_{\mathrm{fg-}}$** are like AP$_{\mathrm{g+}}$ and AP$_{\mathrm{g-}}$ except that the square of Earth's angular velocity is also changed by plus or minus
      20%, respectively, so that the centrifugal force partly compensates the increase in gravity.

The model output consists of instantaneous fields, written at daily intervals (00 UTC), of precipitation, temperature, CWV and vertical velocity at 5 km. The first 100 days of the simulations are discarded for spin-up. After 100 days, global mean outgoing longwave radiation, CWV and precipitation fluctuate around their equilibrium. The last 260 days are subject to the analysis.

2.2 Observations

We analyze instantaneous CWV at hourly intervals from the ERA5 reanalysis (C3S, 2017), and reprocessed and bias-corrected 30-min accumulations of precipitation at hourly intervals from CMORPH (Xie et al., 2019) from 1998 to 2021. ERA5 is provided on a $0.28125° \times 0.28125°$ latitude-longitude grid with a resolution of 31 km at the equator. CMORPH is provided on a $0.0727° \times 0.0727°$ latitude-longitude grid which corresponds to a resolution of 8 km at the equator. For simplicity and to better emphasize the difference with the modeling results, we refer to ERA5 as observations.

2.3 Cluster and island properties

This study focuses on the tropical regions and so only output between 25°S and 25°N is analyzed, and for this purpose regridded from the native 10 km grid to a $0.1° \times 0.1°$ latitude-longitude grid. We process ERA5 and CMORPH in the same way.

We define grid points as precipitating when precipitation rates exceed a threshold of 2 mm h^{-1}. Li et al. (2022) used 0.7 mm h^{-1}, but report that their results were not sensitive to varying the threshold between 0.1 and 2.5 mm h^{-1}. Their study also differs in that they considered 3-hourly averages. A cluster is then defined as a four-point connected precipitating region. We give the area, A, in units of pixels, where one pixel measures $0.1° \times 0.1°$. Latitudinal distortions are small due to confining the analysis to the tropics and hence ignored. For the perimeter length we report the number of pixel edges, such that a single isolated precipitating pixel would have a perimeter of 4. Precipitation cluster volume I is defined as instantaneous precipitation rates integrated over a cluster, i.e. total cluster precipitation, and thus has units of mm h^{-1} pixel. We denote the exponent of the area frequency distribution by α, such that the probability to encounter a cluster with area A is given by $P(A) \sim A^{\alpha}$. Similarly, for the volume I, $P(I) \sim I^{\beta}$. Perimeter λ and volume I are related to area through the fractal dimensions δ_{λ} and δ_{μ}: $\lambda = A^{\delta_{\lambda}/2}$ and $I = A^{\delta_{\mu}/2}$.

We also analyze areas (A) and volumes (V) of CWV islands. Note that we use the symbol I for the volume of precipitation clusters and V for the volume of CWV islands, as these quantities have different units. The volume of a CWV island is the total CWV above a threshold inside the corresponding island area, i.e. for each CWV island we sum the CWV of all pixels above the threshold after subtracting the threshold value. We cut the CWV field at three different thresholds: the 40th and 80th percentiles of the tropical CWV frequency distribution of each data set, and the critical threshold, defined as the CWV where precipitation rates reach 2 mm h^{-1} on average. These critical threshold values are discussed below in Section 3.2. We confine our analysis to columns over the ocean to increase the chance of finding universal behavior across the domains, many of which do not have land, but this only influences the analysis of the CTL simulations and the observations. Areas of CWV clusters are defined in the same way as for precipitation.
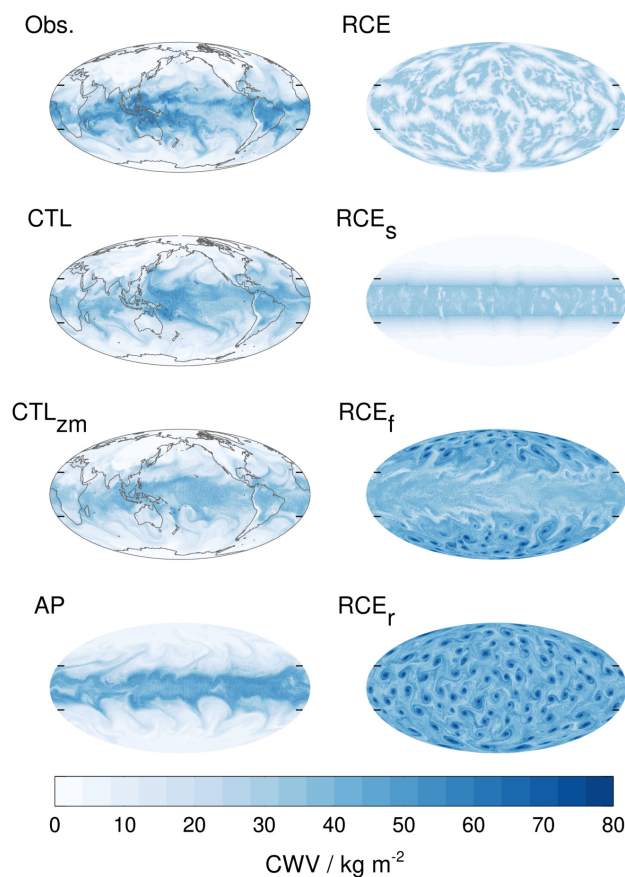
Figure 1. Global maps of CWV. Data from ERA5 (Obs.) show March 1, 2011 00 UTC and the seven experiments show day 100 of the simulations (after spinup). Short lines at the right and left edge of each map mark the tropics ($\pm 25°$).

To estimate the scaling exponents α and β and the fractal dimensions δ_λ and δ_μ, we bin the area and volume data into
120 logarithmic bins and perform a linear regression in log-log space. The logarithmic binning reduces noise in the tails of the distributions. The start and end values of the regression range are chosen to maximize the linear correlation coefficient between the data and the fit, but for a valid fit we require the linear correlation coefficient to be at least 0.999. Additionally, the fit must use at least a quarter of the logarithmic bins. If these criteria cannot be fulfilled, no spectral slope is determined. In the corresponding plots we highlight data points when they fall within 10% of the best-fit line.
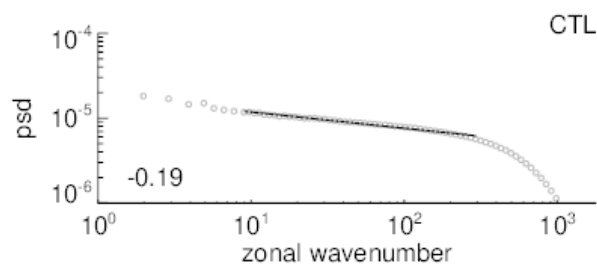
Figure 2. Meridionally averaged power spectral density in units of $m^2 \, s^{-2}$ of vertical velocity at 5 km height for CTL. The slope shown inside the panel is computed for zonal wavenumbers $8 < k < 300$, shown in black.

3 Results

3.1 Dynamics on different scales

Figure 1 shows the global CWV field on day 100 of the simulations and on a randomly chosen date in ERA5 (denoted as Obs.). It documents substantial differences in planetary and synoptic scale variability and in the associated stirring and vertical overturning (macroturbulence) of the atmosphere.

The control simulation CTL with realistic SSTs, land and a diurnal cycle, resembles observations, including enhanced moisture above the warm SSTs of the western tropical Pacific. As expected, this local maximum is absent when zonal mean SSTs are prescribed (CTL_{zm}). The aquaplanet simulation AP has less variability compared to CTL and CTL_{zm}. Still, the effects of planetary and synoptic scale disturbances on the CWV field of AP visibly define a tropical margin.

Moist and dry patches form globally in the radiative-convective equilibrium simulation RCE, indicative of convective self-aggregation (Muller and Held, 2012). RCE_s, which has a meridional SST gradient, produces a band of high CWV at the equator where SSTs are maximum. The CWV band in RCE_s has structures on finer scales compared to RCE. RCE_f, which rotates like Earth, and RCE_r, where the Coriolis parameter is globally set to its value at $45°N$, produce tropical storms where the Coriolis force is nonzero (Held and Zhao, 2008). In RCE_f the CWV field is relatively smooth in the tropics, where the Coriolis parameter is not large enough to support the formation of tropical storms. The CWV field of RCE_f shows planetary and (to a lesser extent) synoptic scale variability in the zonal direction. We do not show the extra AP simulations in Fig. 1, because they look the same modulo differences in amplitude as AP. Differences are discussed in Appendix A.

Vertical velocity spectra are useful for comparing the prevalence of different scales of vertical motion between the simulations. The spectrum of CTL is shown in Fig. 2. The spectra of the other simulations looks similar, differing only in the spectral slope (Appendix B). The slopes of the simulated vertical velocity spectra at zonal wavenumbers $8 < k < 300$ vary between -0.05 (RCE and RCE_s) and -0.24 (RCE_r). Thus, coherent large-scale overturning is most ubiquitous – relative to other scales – in RCE_r, followed by the CTL simulations (CTL: -0.19, CTL_{zm}: -0.17), followed by the AP simulations (between -0.09 and -0.16). The remaining RCE experiments have flatter slopes, which is consistent with a preference for overturning on small
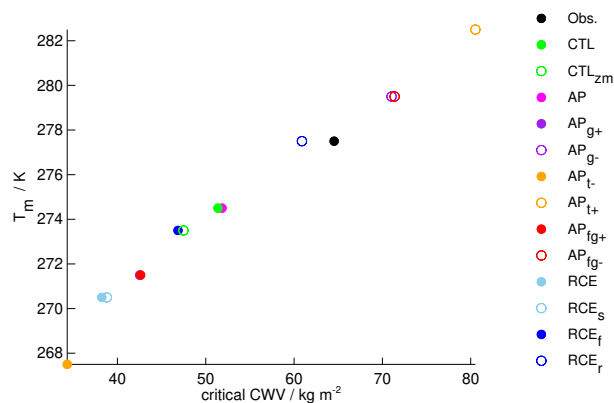
Figure 3. For each data set symbols mark CWV_{crit} corresponding to the most frequently occurring temperature bin T_m.

horizontal scales and relatively weak large-scale dynamics. Next, we examine what these differences imply for the scaling of precipitation clusters.

3.2 Mass flux and cluster size

The CWV threshold for the onset of precipitation depends strongly on tropospheric bulk temperature, defined as mass weighted temperature between 1 and 10 km height. For each data set we define the critical CWV (CWV_{crit}) as the threshold where precipitation rates reach on average 2 mm h^{-1} at the most frequently occurring bulk temperature bin (T_m). Figure 3 shows T_m and CWV_{crit} for our data sets. To proceed with our analysis, we rescale temperature by subtracting T_m and we define reduced CWV as ($CWV-CWV_{crit}$)/CWV_{crit}. Figure 4 shows the precipitation onset lines in the original and normalized phase space. Except for dry or moist outliers, the onset curves collapse onto the same line in the normalized phase space. This is particularly clear for the AP simulations (Fig. 4c,d). For the other simulations (Fig. 4a,b) the change is less impressive because these simulations differ widely in their temperature distributions.

Figure 5 shows a snapshot of a random scene taken from the different configurations. In the simulations with less pronounced large-scale dynamics, isolated, small-scale convection prevails. Panel (b) shows the product of CWV and vertical velocity at 5 km height for the same time as in Fig. 5a. As expected, the product correlates well with the CWV field itself, i.e. ascent occurs predominantly in moist regions. Large positive values in Fig. 5b are indicative of strong mass flux. Stronger mass flux can be realized either through stronger ascent within same-sized convective areas, or through an increase in area coverage. Previous studies demonstrated that nature follows the second option due to microphysical constraints (Doneaud et al., 1984; Nuijens et al., 2009; Parodi et al., 2011; Fildier et al., 2017). Our simulations agree with their results, as Fig. 6 demonstrates. It shows the dependence of cluster area on reduced CWV for our data sets and in addition it shows the average precipitation rate inside clusters, i.e. volume divided by area. With increasing CWV_{crit}, area size increases more rapidly than the average precipitation
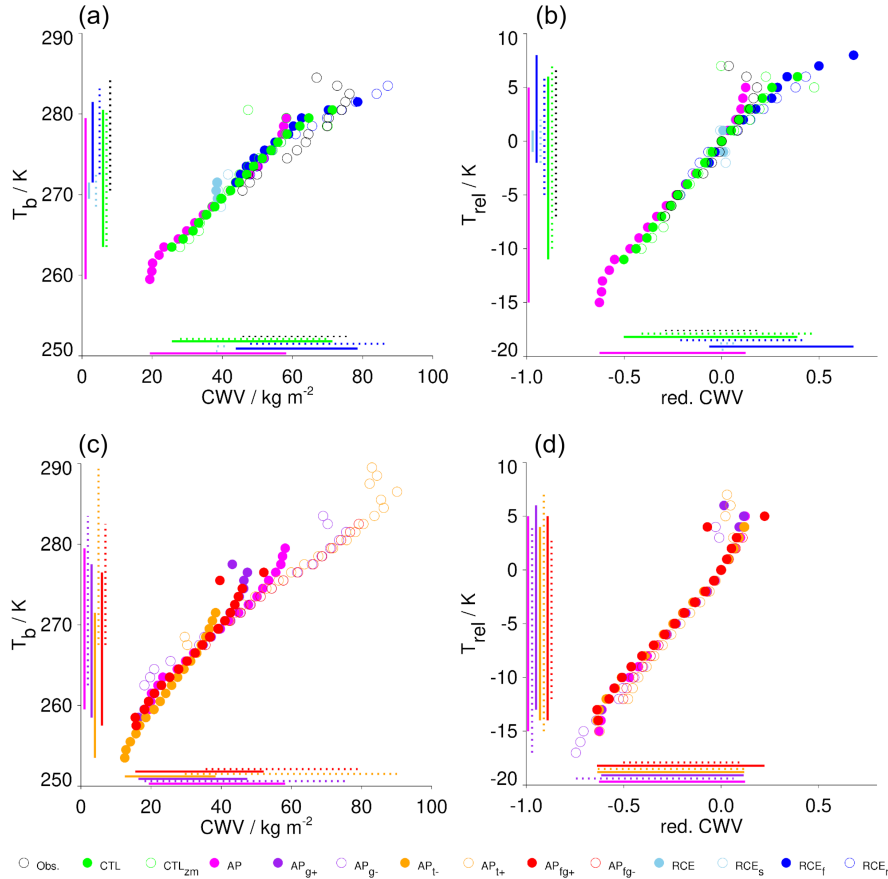
Figure 4. Precipitation onset curves. In (a) and (c) an open or filled circle marks the average CWV at which precipitation rates reach 2 mm h^{-1} for each bulk temperature (y-axis). Lines along the axes mark the range covered by the respective 2 mm h^{-1} isoline of a simulation. (b) and (d) repeat (a) and (c) in the phase space of reduced CWV and relative temperature.

rate. However, the difference in growth rates is much more pronounced in CTL and RCE$_r$, whereas it is substantially smaller in the other RCE simulations. This is again due to the presence of stronger large-scale dynamics and greater mass flux.

170   We now turn to the question to what extent different dynamics influence the area-size distributions of precipitation clusters and CWV islands.

3.3 Precipitation clusters and CWV islands

Figure 7 shows the occurrence frequency spectra of areas for CWV islands and precipitation clusters. The corresponding slopes of all data sets are summarized in Fig. 8a whenever a fit was possible. The occurrence frequency spectra for volumes are shown

175   in Appendix C. Focusing first on observations, CMORPH precipitation follows a slope of -1.79 for area (gray star in the leftmost column of Fig. 8a). The CWV islands of ERA5 cannot be expected to follow any scaling law at fine scales, as ERA5's
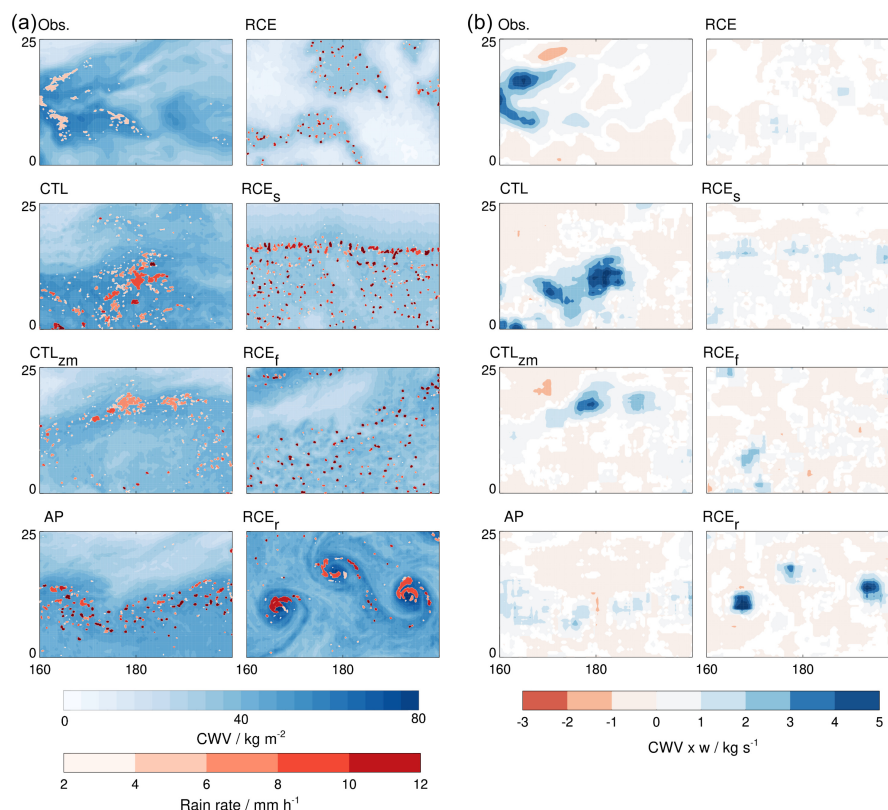
Figure 5. Snapshots of moisture fields. (a) shows CWV and cluster-mean precipitation rate on day 100 of the simulations and on March 1, 2011 00 UTC in observations. The y-axis shows latitude in °N and the x-axis shows longitude in °E. (b) shows for the same times CWV multiplied by the vertical velocity at 5 km height. Before multiplication both fields were smoothed with a 390 km boxcar filter. Values between -0.1 and 0.1 kg s^{-1} are colored white.

horizontal resolution is a factor of ~4 coarser than that of CMORPH. For the 40% and 80% thresholds, the area scalings in ERA5 are flatter (40%: -1.62, 80%: -1.41) than those of precipitation, but at the critical threshold the slope is steeper (-1.87). Differences in the slopes of CWV and precipitation volumes (Fig. 8b) are similar to those in the area distributions.

180   By visual inspection of Fig. 7, CTL and CTL$_{zm}$ show the best overall agreement of CWV and precipitation spectra with observations, when we consider all scales. It should be noted that the cluster statistics for CTL and CTL$_{zm}$ suffer from the fact that clusters touching land have to be discarded. This causes noisy tails. In ERA5 this effect is compensated by the amount of data spanning 24 years. It appears that the simulated spectra, particularly those of precipitation, have a slight bias towards small scales. A local maximum in the spectra can be seen even in CTL. It is common that simulations tend to preferentially form

185 small precipitation clusters that rain too heavily when using an explicit representation of moist convection at what is still rather coarse resolution (Becker et al., 2021). The snapshot of a random scene shown in Fig. 5a illustrates this point. It is conceivable that looking at instantaneous data of the simulations versus 30-min averaged data of CMORPH explains some of these biases.
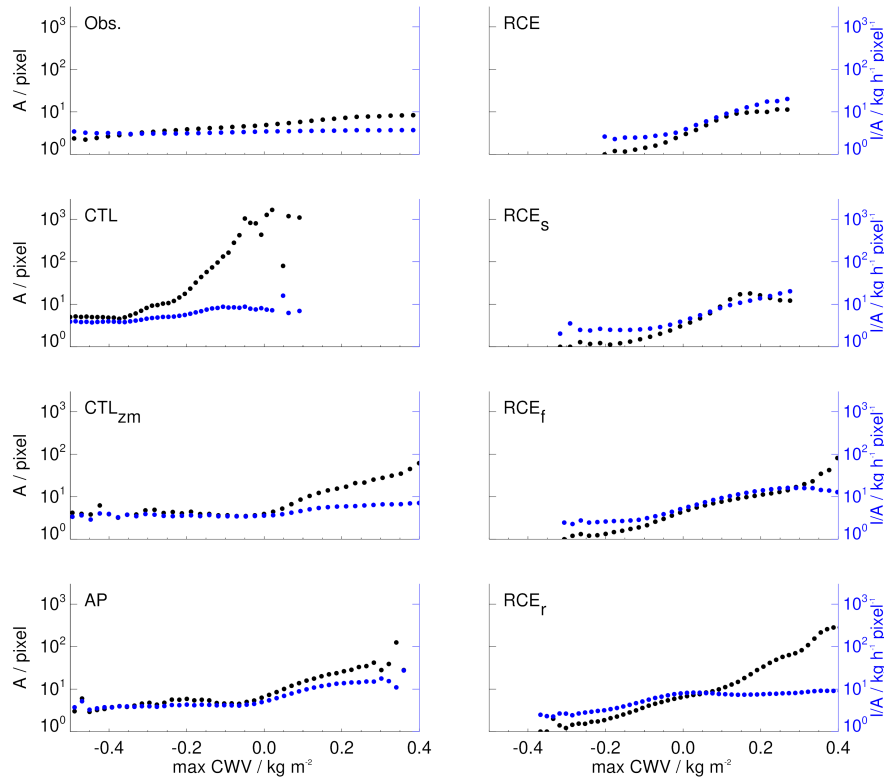
Figure 6. The average precipitation cluster area (black) and volume divided by area (blue) as function of the maximum reduced CWV value inside a cluster.

Moreover, precipitation is not directly measured by remote sensing instruments but estimated from infrared measurements of column condensate path, which might introduce some additional smoothing (Pradhan et al., 2022).

190   The curves for the CWV areas of all AP simulations resemble the CTL simulations, with precipitation areas following steeper curves than CWV island areas, as in CTL. Finally, the RCE simulations vary greatly in the degree of similarity between spectra at different CWV thresholds and those of precipitation. The tropical storms in RCE_r introduce a scale of organization, which is on the order of 200 km (Fig. 5a). It matches the peak in the precipitation area distribution of Fig. 7 at ~500 pixel, which corresponds to a linear scale of $\sqrt{500 \times 10^2} \approx 224$ km. The coherent upward motion must be compensated by subsidence

195   on scales ≥ 224 km. In contrast, in RCE, RCE_s and RCE_f, precipitation occurs in moist patches as isolated, small scale convection, creating updrafts on small horizontal scales, but also downwelling on smaller scales. Hence, in RCE, RCE_s and RCE_f, the small-scale dynamics decouple from the large-scale distribution of the CWV field. This is seen in the diverging curves of Fig. 7. Weak and slowly varying overturning only shapes large-scale dry and moist patches.

    In contrast, with steeper vertical velocity spectra, there is an increasingly better match between the scalings of islands at

200   all thresholds and precipitation. This also holds for the AP experiments. The warmer AP simulations have a better match and
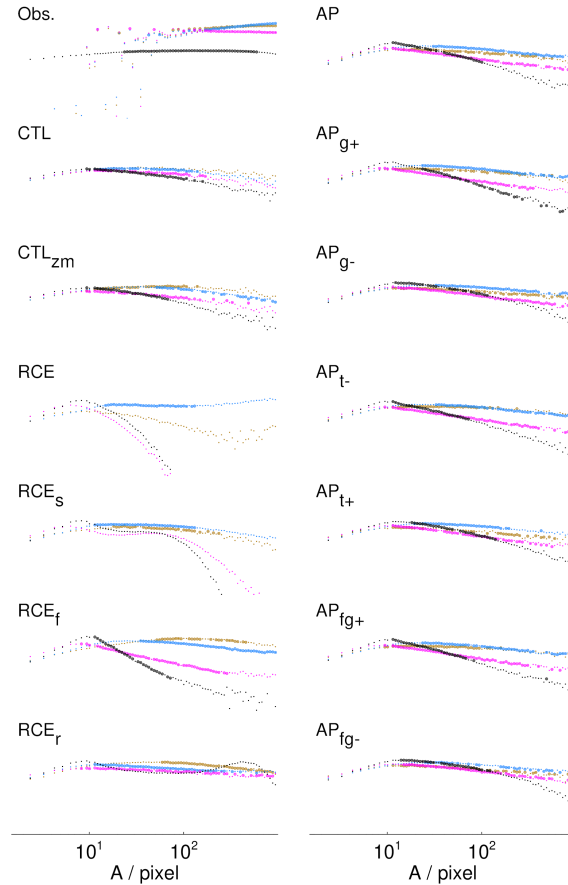
Figure 7. Occurrence frequencies of areas belonging to precipitation clusters (black) and CWV islands at the 40% threshold (brown), the 80% threshold (blue), and the critical threshold (magenta). All curves are compensated by $A^{1.79}$. Thick dots mark the intervals with the best power law (Section 2.3).

steeper slopes (AP_{g-}: -0.15, AP_{t+}: -0.12, AP_{fg-}: -0.16) than AP (-0.11) and than the colder experiments, which have flatter slopes (AP_{g+}: -0.09, AP_{t-}: -0.10, AP_{fg+}: -0.09).

3.4 Roughness exponent

We found evidence that the presence of large-scale dynamics, or a steep slope of the vertical velocity spectrum, is required for cluster areas and volumes to follow distributions with approximately constant slope, but this does not answer what this slope should be. As mentioned in Section 1, the KPZ equation (Eq. 1) predicts $h \approx 0.3867$. For self-affine surfaces, the slopes for area and volume occurrence (α, β) and the fractal dimensions (δ_λ, δ_μ) are related to h. The area scaling exponent α is given by $\alpha = h/2 - 2$ (Pelletier, 1997). Li et al. (2022) derived for β the relationship $\beta = -4/(2 + h)$, Kondev and Henley (1995)
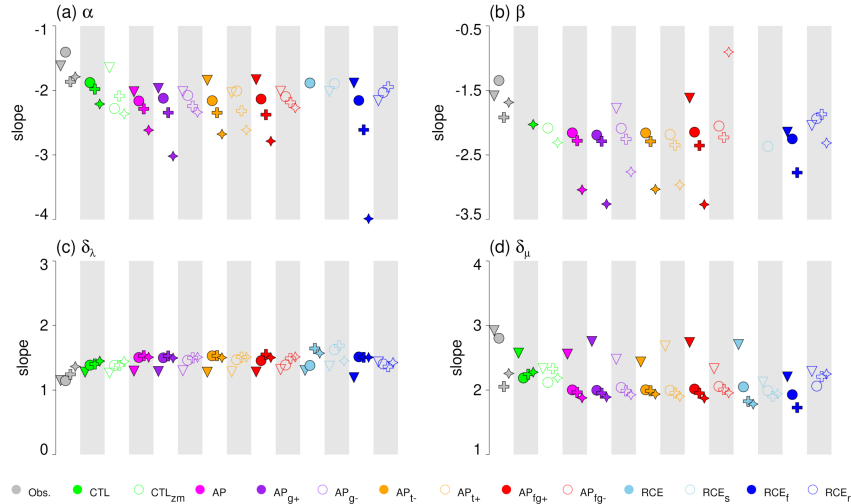
Figure 8. Slopes obtained from fitting a scaling law to the data shown in Figs 7, C1, C2 and C3. Each column shows a different data set identified by filled or unfilled colors as shown by the legend at the bottom. Each column can have four symbols, where the star stands for precipitation, the downward pointing triangle for the 40% CWV threshold, the circle for the 80% threshold, and the plus for the critical threshold. A missing symbol implies that a fit could not be obtained.

showed $\delta_\nu = (3 - h)/2$, and Li et al. (2022) $\delta_\mu = 2 + h$. Table 1 lists α, β, δ_λ and δ_μ for different values of the roughness

210 exponent h. Plots of the fractal dimensions are shown in Appendix C.

Table 1. Scaling exponents and fractal dimensions. The rows list the scaling exponents (α, β) and fractal dimensions (δ_λ, δ_μ) for different roughness exponents (h), and those obtained for CMORPH and the CTL simulation.

	$h = 0.4$	$h = 0.3$	$h = 0$	$h = 1$	CMORPH	CTL
α	-1.80	-1.85	-2.00	-1.50	-1.79	-2.21
β	-1.67	-1.74	-2.00	-1.33	-1.69	-2.03
δ_λ	1.30	1.35	1.50	1.00	1.36	1.45
δ_μ	2.40	2.30	2.00	3.00	2.26	2.28

CMORPH precipitation clusters and simulated clusters agree much better in terms of their fractal dimensions than they do in terms of area or volume distributions (Fig. 8). The better agreement in δ_λ and δ_μ compared to α and β between the simulations suggests that the fractal dimensions might be controlled by turbulence, as was also proposed by previous studies (Garrett et al., 2018; Siebesma and Jonker, 2000).

4 Conclusions

Based on simulations of Earth-like and un-Earth-like planets we searched for ingredients that are required to have precipitation clusters follow scaling laws. Key is the presence of stirring and large-scale vertical overturning as associated with substantial planetary and synoptic-scale variability. The presence of such large-scale dynamics is reflected in steep vertical velocity spectra. Large-scale rising and sinking modulate the column water vapor (CWV) and temperature field, leading to a heterogeneous distribution of moist and dry patches and regions of strong mass flux, in which large precipitation clusters form. A dearth of large-scale structures, as reflected in flat vertical velocity spectra, is associated with a decoupling of the large-scale distribution of CWV and precipitation. In this latter scenario, weak overturning shapes large-scale dry and moist patches, and only weak mass flux is present in the moist patches. Precipitation is then realized as unorganized isolated convection.

The global motion spectrum is strongly shaped by the distribution of orography and the presence of rotation and differential heating, with convection contributing mainly to the mesoscale motion spectrum (Stephan et al., 2019a, b; Köhler et al., 2023). Horizontal motion spectra follow robust scaling laws (Stephan et al., 2022), which also determine the spectra of vertical motion (Morfa Avalos and Stephan, 2023) and horizontal divergence (Stephan and Mariaccia, 2021). Our finding that the structure of Earth's motion field is important to having precipitation clusters follow scaling laws implies that any potential applicability of the Kardar-Parisi-Zhang (KPZ) equation to the problem of Earth's CWV field relies on the coincidence of the noise term η in Eq. 1 agreeing with the properties of Earth's motion spectra. Whether KPZ dynamics are applicable or not, our results show that precipitation cluster statistics derive their apparent universality from the robust spectral characteristics of atmospheric wave and turbulence dynamics.

Code and data availability. CMORPH data can be obtained from the National Centers for Environmental Information's National Oceanic and Atmospheric Administration. The ERA5 reanalysis is produced and made publicly available by the ECMWF. The ICON model (ICON-partnership, 2024) is open source. More information about ICON is available at https://www.icon-model.org/. The versions of the code used for the simulations analyzed here are uniquely identified by their git hashes. They are: 0a47ce01ee3c6dada56e21b17da66f54499db3e3 for CTL and CTL$_{zm}$ and 0d09a39ed159c51cf6f8ce5c654cf206c8c037c5 for all other simulations.

Appendix A: Aquaplanet simulations

In the extra aquaplanet simulations the SSTs were globally increased (AP$_{t+}$) or decreased (AP$_{t-}$), gravity was increased (AP$_{g+}$) or decreased (AP$_{g-}$), and gravity together with the Coriolis parameter were increased (AP$_{fg+}$) or decreased (AP$_{fg-}$). The zonal mean CWV of the AP simulations is compared in Fig. A1. AP$_{t+}$ is warmer than AP and therefore contains more CWV in the tropics. AP$_{t-}$ behaves in the opposite way. In addition, Fig. A1 shows that the CWV peaks are further apart in AP$_{t+}$, indicative of broader tropics, and less apart in AP$_{t-}$. AP$_{g-}$ and AP$_{fg-}$ look nearly the same. They contain almost as much CWV as AP$_{t+}$, with CWV maxima closer to the equator than AP. Similarly, AP$_{g+}$ and AP$_{fg+}$ are colder than AP with peaks further away from the equator.
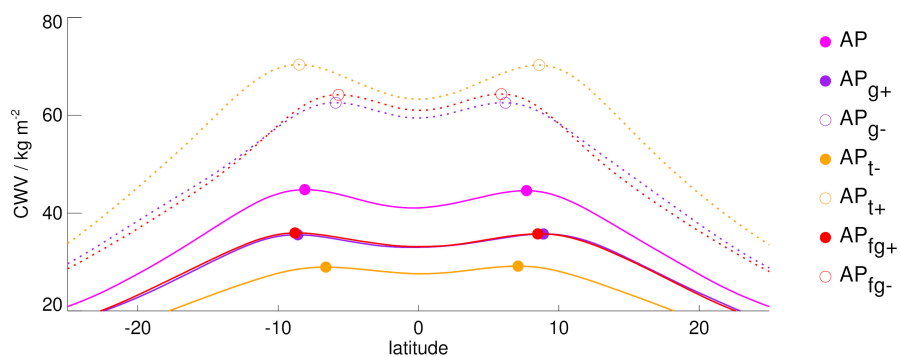
Figure A1. Zonal-mean time-mean CWV in the tropics as simulated by the aquaplanet simulations. Open or filled circles mark the respective maximum in each hemisphere to facilitate the comparison.

Appendix B: Vertical velocity spectra
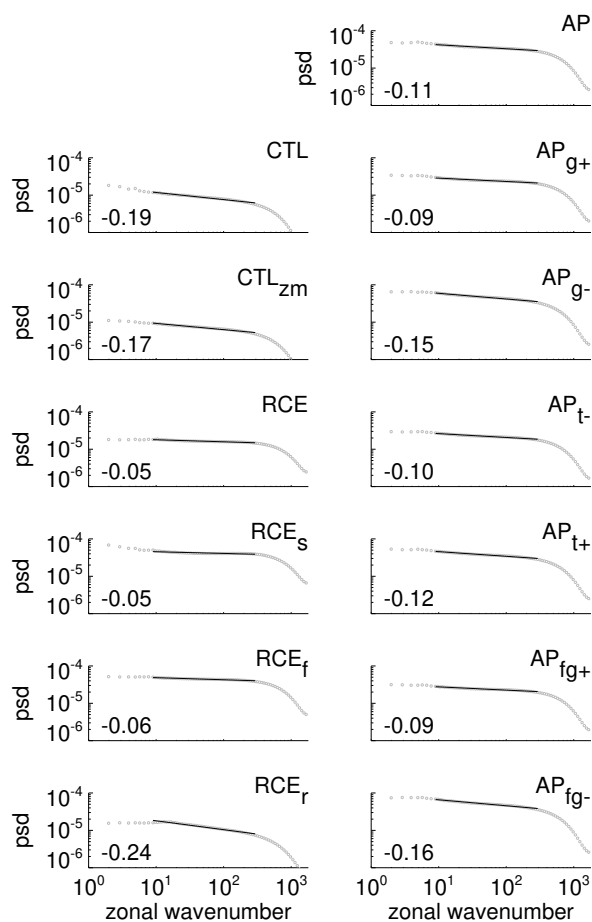
Figure B1. Meridionally averaged power spectral density in units of m^2 s^{-2} of vertical velocity at 5 km height. Slopes shown inside the panels are computed for zonal wavenumbers $8 < k < 300$, shown in black. All displayed decimal places are one order of magnitude larger than their one-sigma uncertainty estimates.

Appendix C: Cluster properties
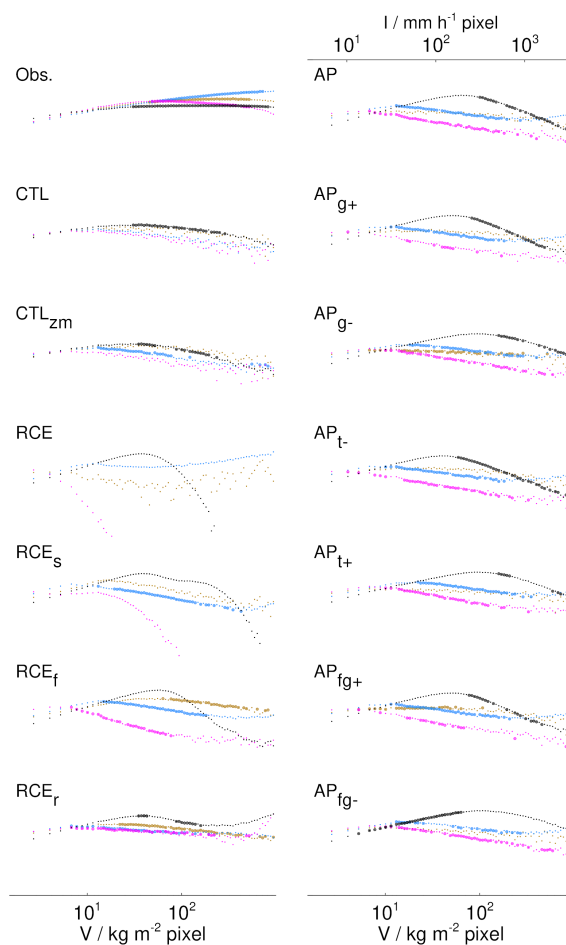
Figure C1. Occurrence frequencies of precipitation volume I or CWV volume V belonging to precipitation clusters (black) and CWV islands at the 40% threshold (brown), the 80% threshold (blue), and the critical threshold (magenta). Thick dots mark the intervals with the best power law. All curves are compensated by $(I \text{ or } V)^{1.69}$. Colors are as in Fig. 7.
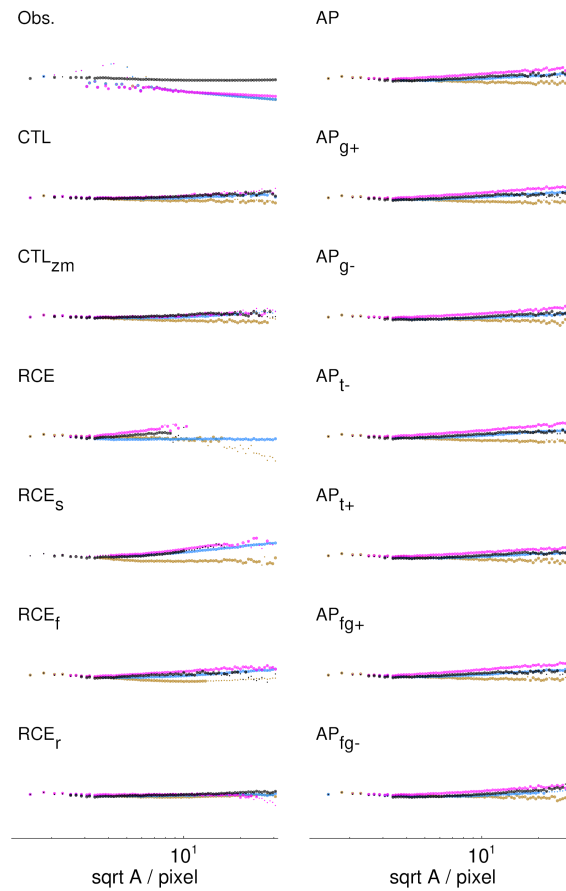
Figure C2. Fractal dimensions of precipitation clusters and CWV islands. Shown is circumference λ versus $\sqrt{A}$. All spectra are compensated by $\sqrt{A}^{-1.36}$. Colors are as in Fig. 7.
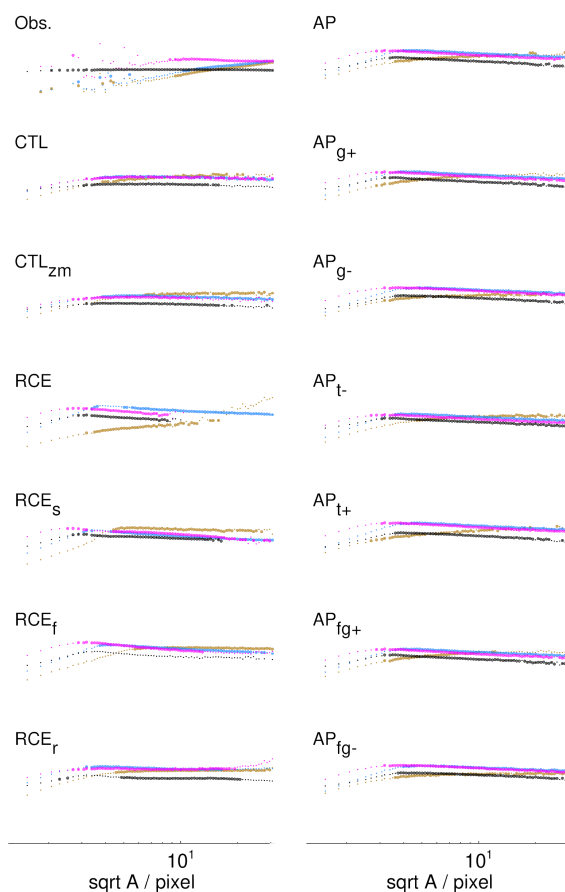
Figure C3. Fractal dimensions of precipitation clusters and CWV islands. Shown is precipitation volume I or CWV volume V, respectively, versus $\sqrt{A}$. All spectra are compensated by $\sqrt{A}^{-2.26}$. Colors are as in Fig. 7.

Author contributions. The authors contributed equally to the conceptualization of the work. CCS performed most of the analysis and writing of the original draft with inputs from BS.

250 *Competing interests.* The authors declare that they have no competing interests.

Acknowledgements. CCS carried out the research when she was still working at the Max Planck Institute for Meteorology and supported by the Minerva Fast Track programme of the Max Planck Society.

References

Ahmed, F. and Neelin, J. D.: Explaining Scales and Statistics of Tropical Precipitation Clusters with a Stochastic Model, J. Atmos. Sci., 76, 3063–3087, https://doi.org/10.1175/JAS-D-18-0368.1, 2019.

Becker, T., Bechtold, P., and Sandu, I.: Characteristics of convective precipitation over tropical Africa in storm-resolving global simulations, Quart. J. Roy. Meteor. Soc., 147, 4388–4407, https://doi.org/10.1002/qj.4185, 2021.

C3S: ERA5: Fifth generation of ECMWF atmospheric reanalyses of the global climate. Copernicus Climate Change Service Climate Data Store (CDS), Last accessed: November 2020, https://cds.climate.copernicus.eu/cdsapp#!/home, 2017.

Doneaud, A. A., Ionescu-Niscov, S., Priegnitz, D. L., and Smith, P. L.: The Area-Time Integral as an Indicator for Convective Rain Volumes, J. Applied Meteor Climatology, 23, 555–561, https://doi.org/10.1175/1520-0450(1984)023<0555:TATIAA>2.0.CO;2, 1984.

Fildier, B., Parishani, H., and Collins, W. D.: Simultaneous characterization of mesoscale and convective-scale tropical rainfall extremes and their dynamical and thermodynamic modes of change, J. Adv. Model. Earth Syst., 9, 2103—-2119, https://doi.org/10.1002/2017MS001033, 2017.

Garrett, T. J., Glenn, I. B., and Krueger, S. K.: Thermodynamic Constraints on the Size Distributions of Tropical Clouds, J. Geophys. Res. Atm., 123, 8832–8849, https://doi.org/10.1029/2018JD028803, 2018.

Hagemann, S. and Stacke, T.: Impact of the soil hydrology scheme on simulated soil moisture memory, Clim. Dyn., 44, 1731—-1750, https://doi.org/10.1007/s00382-014-2221-6, 2015.

Held, I. M. and Zhao, M.: Horizontally Homogeneous Rotating Radiative–Convective Equilibria at GCM Resolution, J. Atmos. Sci., 65, 2003–2013, https://doi.org/10.1175/2007JAS2604.1, 2008.

Hohenegger, C., Korn, P., Linardakis, L., Redler, R., Schnur, R., Adamidis, P., Bao, J., Bastin, S., Behravesh, M., Bergemann, M., Biercamp, J., Bockelmann, H., Brokopf, R., Brüggemann, N., Casaroli, L., Chegini, F., Datseris, G., Esch, M., George, G., Giorgetta, M., Gutjahr, O., Haak, H., Hanke, M., Ilyina, T., Jahns, T., Jungclaus, J., Kern, M., Klocke, D., Kluft, L., Kölling, T., Kornblueh, L., Kosukhin, S., Kroll, C., Lee, J., Mauritsen, T., Mehlmann, C., Mieslinger, T., Naumann, A. K., Paccini, L., Peinado, A., Praturi, D. S., Putrasahan, D., Rast, S., Riddick, T., Roeber, N., Schmidt, H., Schulzweida, U., Schütte, F., Segura, H., Shevchenko, R., Singh, V., Specht, M., Stephan, C. C., von Storch, J.-S., Vogel, R., Wengel, C., Winkler, M., Ziemen, F., Marotzke, J., and Stevens, B.: ICON-Sapphire: simulating the components of the Earth system and their interactions at kilometer and subkilometer scales, Geosci. Model Dev., 16, 779–811, https://doi.org/10.5194/gmd-16-779-2023, 2023.

Holloway, C. E., Woolnough, S. J., and Lister, G. M. S.: Precipitation distributions for explicit versus parametrized convection in a large-domain high-resolution tropical case study, Quart. J. Roy. Meteor. Soc., 138, 1692–1708, https://doi.org/https://doi.org/10.1002/qj.1903, 2012.

ICON-partnership: ICON release 2024.01, https://doi.org/10.35089/WDCC/IconRelease01, 2024.

Kardar, M., Parisi, G., and Zhang, Y.-C.: Dynamic Scaling of Growing Interfaces, Phys. Rev. Lett., 56, 889–892, https://doi.org/10.1103/PhysRevLett.56.889, 1986.

Kinne, S.: Aerosol radiative effects with MACv2, Atmos. Chem. Phys., 19, 10 919–10 959, https://doi.org/10.5194/acp-19-10919-2019, 2019.

Kondev, J. and Henley, C. L.: Geometrical Exponents of Contour Loops on Random Gaussian Surfaces, Phys. Rev. Lett., 74, 4580–4583, https://doi.org/10.1103/PhysRevLett.74.4580, 1995.

Köhler, L., Green, B., and Stephan, C.: Comparing Loon superpressure balloon observations of gravity waves in the tropics with global storm-resolving models, J. Geophys. Res.: Atmospheres, 128, e2023JD038 549, https://doi.org/10.1029/2023JD038549, 2023.

290   Li, Z., O'Gorman, P. A., and Rothman, D. H.: Tropical precipitation clusters as islands on a rough water-vapor topography, Quart. J. Roy. Meteor. Soc., 148, 403–417, https://doi.org/10.1002/qj.4211, 2022.

Meinshausen, M., Vogel, E., Nauels, A., Lorbacher, K., Meinshausen, N., Etheridge, D., Fraser, P., Montzka, S. A., Rayner, P., Trudinger, C., Krummel, P., Beyerle, U., Canadell, J. G., Daniel, J. S., Enting, I., Law, R. M., OD́oherty, S., Prinn, R. G., Reimann, S., Rubino, M., Vollmer, M. K., and Weiss, R.: Historical greenhouse gas concentrations, https://doi.org/10.5194/gmd-2016-169, 2016.

295   Morfa Avalos, Y. A. and Stephan, C. C.: The relationship between horizontal and vertical velocity wavenumber spectra in global storm-resolving simulations, J. Atmos. Sci., 80, 1087—1105, https://doi.org/10.1175/JAS-D-22-0105.1, 2023.

Muller, C. J. and Held, I. M.: Detailed investigation of the self-aggregation of convection in cloud-resolving simulations, J. Atmos. Sci., 69, 2551–2565, https://doi.org/10.1175/JAS-D-11-0257.1, 2012.

Neale, R. B. and Hoskins, B. J.: A standard test for AGCMs including their physical parametrizations: I: The proposal, Atmos. Sci. Lett., 1,
300   101–107, https://doi.org/10.1006/asle.2000.0019, 2000.

Nuijens, L., Stevens, B., and Siebesma, A. P.: The Environment of Precipitating Shallow Cumulus Convection, J. Atmos. Sci., 66, 1962–1979, https://doi.org/10.1175/2008JAS2841.1, 2009.

Pagnani, A. and Parisi, G.: Numerical estimate of the Kardar-Parisi-Zhang universality class in (2+1) dimensions, Phys. Rev. E, 92, 010 101, https://doi.org/10.1103/PhysRevE.92.010101, 2015.

305   Parodi, A., Foufoula-Georgiou, E., and Emanuel, K.: Signature of microphysics on spatial rainfall statistics, J. Geophys. Res., 116, D14119, https://doi.org/10.1029/2010JD015124, 2011.

Pelletier, J. D.: Kardar-Parisi-Zhang Scaling of the Height of the Convective Boundary Layer and Fractal Structure of Cumulus Cloud Fields, Phys. Rev. Lett., 78, 2672–2675, https://doi.org/10.1103/PhysRevLett.78.2672, 1997.

Peters, O. and Neelin, J. D.: Critical phenomena in atmospheric precipitation, Nature Phys., 2, 393–396, https://doi.org/10.1038/nphys314,
310   2006.

Peters, O., Neelin, J. D., and Nesbitt, S. W.: Mesoscale Convective Systems and Critical Clusters, J. Atmos. Sci., 66, 2913–2924, https://doi.org/10.1175/2008JAS2761.1, 2009.

Peters, O., Deluca, A., Corral, A., Neelin, J. D., and Holloway, C. E.: Universality of rain event size distributions, J. Stat. Mech.: Theory and Experiment, p. P11030, https://doi.org/10.1088/1742-5468/2010/11/P11030, 2010.

315   Pradhan, R. K., Markonis, Y., Vargas Godoy, M. R., Villalba-Pradas, A., Andreadis, K. M., Nikolopoulos, E. I., Papalexiou, S. M., Rahim, A., Tapiador, F. J., and Hanel, M.: Review of GPM IMERG performance: A global perspective, Remote Sensing of Environment, 268, 112 754, https://doi.org/10.1016/j.rse.2021.112754, 2022.

Quinn, K. M. and Neelin, J. D.: Distributions of Tropical Precipitation Cluster Power and Their Changes under Global Warming. Part I: Observational Baseline and Comparison to a High-Resolution Atmospheric Model, J. Climate, 30, 8033–8044, https://doi.org/10.1175/JCLI-
320   D-16-0683.1, 2017a.

Quinn, K. M. and Neelin, J. D.: Distributions of Tropical Precipitation Cluster Power and Their Changes under Global Warming. Part II: Long-Term Time Dependence in Coupled Model Intercomparison Project Phase 5 Models, J. Climate, 30, 8045–8059, https://doi.org/10.1175/JCLI-D-16-0701.1, 2017b.

Schemann, V., Stevens, B., Gruetzun, V., and Quaas, J.: Scale dependency of total water variance and its implication for cloud parameteriza-
325   tions, J. Atmos. Sci., pp. 3615–3630, https://doi.org/10.1175/JAS-D-13-09.1, 2013.

Siebesma, A. P. and Jonker, H. J. J.: Anomalous Scaling of Cumulus Cloud Boundaries, Phys. Rev. Lett., 85, 214–217, https://doi.org/10.1103/PhysRevLett.85.214, 2000.

Stephan, C. and Mariaccia, A.: The signature of the tropospheric gravity wave background in observed mesoscale motion, Weather Clim. Dynam., 2, 359—372, https://doi.org/10.5194/wcd-2-359-2021, 2021.

330 Stephan, C., Strube, C., Klocke, D., Ern, M., Hoffmann, L., Preusse, P., and Schmidt, H.: Intercomparison of gravity waves in global convection-permitting models, J. Atmos. Sci., 76, 2739—2759, https://doi.org/10.1175/JAS-D-19-0040.1, 2019a.

Stephan, C. C., Strube, C., Klocke, D., Ern, M., Hoffmann, L., Preusse, P., and Schmidt, H.: Gravity waves in global high-resolution simulations with explicit and parameterized convection, J. Geophys. Res., 124, 4446–4459, https://doi.org/10.1029/2018JD030073, 2019b.

Stephan, C. C., Duras, J., Harris, L., Klocke, D., Putman, W. M., Taylor, M., Wedi, N. P., Žagar, N., and Ziemen, F.: At-
335 mospheric energy spectra in global kilometre-scale models, Tellus A: Dynamic Meteorology and Oceanography, 74, 280—299, https://doi.org/10.16993/tellusa.26/, 2022.

Takasuka, D., Kodama, C., Suematsu, T., Ohno, T., Yamada, Y., Seiki, T., Yashiro, H., Nakano, M., Miura, H., Noda, A. T., Na-suno, T., Miyakawa, T., and Masunaga, R.: How Can We Improve the Seamless Representation of Climatological Statistics and Weather Toward Reliable Global K-Scale Climate Simulations?, Journal of Advances in Modeling Earth Systems, 16, e2023MS003 701,
340 https://doi.org/https://doi.org/10.1029/2023MS003701, 2024.

Taylor, K. E., Williamson, D., and Zwiers, F.: The sea surface temperature and sea ice concentration boundary conditions for AMIP II simulations. PCMDI Report 60, Program for Climate Model Diagnosis and Intercomparison, Lawrence Livermore National Laboratory, p. 25, https://doi.org/https://pcmdi.llnl.gov/report/pdf/60.pdf?id=86, 2000.

Teo, C.-K., Huynh, H.-N., Koh, T.-Y., Cheung, K. K. W., Legras, B., Chew, L. Y., and Norford, L.: The universal scaling characteristics of
345 tropical oceanic rain clusters, J. Geophys. Res. Atmos., 122, 5582–5599, https://doi.org/10.1002/2016JD025921, 2017.

Vergara-Temprado, J., Ban, N., Panosetti, D., Schlemmer, L., and Schär, C.: Climate Models Permit Convection at Much Coarser Resolutions Than Previously Considered, Journal of Climate, 33, 1915–1933, https://doi.org/10.1175/JCLI-D-19-0286.1, 2020.

Wing, A. A., Reed, K. A., Satoh, M., Stevens, B., Bony, S., and Ohno, T.: Radiative–convective equilibrium model intercomparison project, Geosci. Mod. Dev., 11, 793–813, https://doi.org/10.5194/gmd-11-793-2018, 2018.

350 Xie, P., Joyce, R., Wu, S., Yoo, S.-H., Yarosh, Y., Sun, F., and Lin, R.: NOAA CDR Program, NOAA Climate Data Record (CDR) of CPC Morphing Technique (CMORPH) High Resolution Global Precipitation Estimates, Version 1 30 min 8 km. NOAA National Centers for Environmental Information. Last accessed: May 7, 2021, https://doi.org/10.25921/w9va-q159, 2019.